Dynamical core-hole screening in the x-ray absorption spectra of graphite, C_{60}, and carbon nanotubes: A first-principles electronic structure study

O. Wessely and O. Eriksson
Department of Physics, Uppsala University, Box 530, SE-75121, Uppsala, Sweden

M. I. Katsnelson
Institute for Molecules and Materials, Radboud University Nijmegen, NL-6525 ED Nijmegen, The Netherlands
(Received 14 September 2005; revised manuscript received 23 November 2005; published 1 February 2006)

We have implemented the effect of dynamical core-hole screening into a first principles electronic structure computational scheme. The method has been applied to the x-ray absorption spectrum of the carbon *K*-edge for graphite, fullerene C_{60} molecules, and single-wall carbon nanotubes. We demonstrate that a theory that includes dynamic core-hole screening improves drastically the description of the experimental data in comparison with both initial- and final-state calculations. Most of the experimentally observed spectral features are well described by our theory, both regarding the position, shape, and relative intensity of the peaks.

DOI: 10.1103/PhysRevB.73.075402 PACS number(s): 73.22.−f, 78.70.Dm, 71.20.−b

I. INTRODUCTION

A. General background

X-ray absorption (XA) spectroscopy has been an active field of research for several decades, both experimentally and theoretically.[1–3] A theoretical interpretation of the experimental observations is still an unsolved problem. The reason is that XA spectroscopy involves very complicated dynamical many-body processes.[1,4] Model calculations have been used successfully to gain qualitative understanding of the XA process in the framework of the Mahan-Nozières-De Dominicis (MND) theory of the dynamical core-hole screening (see, e.g., Refs. 4–6). In particular, we mention the work of Privalov *et al.*[7], who reduce the MND equation to a set of linear algebraic equations, and applied this to a one-dimensional tight-binding model. In order to obtain quantitative information, the XA spectra have often been compared to first-principles calculations (that are based on density functional theory, DFT), both in the initial- and final-state configuration,[8] although it should be noted that the Kohn-Sham eigenvalues, strictly speaking, do not represent dynamical quasiparticle states visible in the spectroscopy. For many materials this approach has limitations, not least due to correlation effects which are not normally taken into account in a standard first-principles electronic structure theory.[2,9] Nevertheless, sometimes the agreement between the first-principles theory and experiment is good,[10] and we note in particular that the optical conductivity of graphite is reproduced with great accuracy using DFT.[11] This means that in this case the Kohn-Sham eigenvalues are rather close to the quasiparticle energies. The fact that so many properties of graphite, C_{60}, and nanotubes are well described using DFT[12–18] motivates using this as a starting point for a calculation of the x-ray absorption spectrum. In order to incorporate dynamical core-hole screening in an element-specific theory we have previously combined the MND theory with *ab initio* electronic structure calculations and some results have been published by us preliminarily in Ref. 19. Here we present a full account of our development of a realistic multiband case of the MND theory.

Quite often the XA spectrum is interpreted in terms of either the initial-state density of states (without core hole) or the final-state density of states (with core hole). The first approach assumes that the interaction of the x-ray photon with the electronic subsystem is very fast in comparison with any typical processes in the latter (such as the electron hopping). The second approach assumes that the photon-electron interaction is adiabatic so that the system transfers from an "old" ground state into the new one. The MND theory considers the creation of the core hole as an instant process but takes into account the real dynamics of the response of the electronic subsystem. As a result, many-body effects due to correlations of electrons with the core hole are included in this theory, and it is in principle better than the initial-state spectra or the final-state spectra. We exemplify our theoretical development with three materials, graphite, C_{60}, and carbon nanotubes. We have chosen these three systems since a lot of attention has been paid to them experimentally, and as will be shown here standard electronic structure theory fail in describing their x-ray absorption spectra.

B. XA spectra for graphite, C_{60}, and carbon nanotubes: Formulation of the problem

As mentioned above, the electronic structure of graphite has attracted attention during a long period and therefore graphite can be considered as one of the basic model systems for core-level spectroscopy. More recently the efforts in trying to understand the electronic properties of different forms of carbon have been intensified enormously due to the discovery of the fullerene C_{60} molecule[20] and the carbon nanotubes.[21] Much attention has been drawn to experiments using the x-ray absorption spectroscopy (XAS) probe on graphite,[22,23] C_{60} (Refs. 24–27) and single-wall carbon nanotubes (SWCNTs),[28,29] and it is clear now that a theoretical interpretation of these data is a difficult problem.

The electronic structure of graphite has also been carefully calculated and analyzed in great detail in Refs. [11,30–33]. It was found that the XA spectrum of graphite can be inter-

preted as a π^* contribution from p_z orbitals and a σ^* contribution from sp^2 hybrid orbitals,[22,23] both of them having mostly excitonic character.[34] A first-principles study[35] demonstrated that the π^* component of the XA spectrum was reproduced when a core hole was simulated by electronic structure calculations for a nitrogen impurity in a supercell of carbon atoms, in an attempt to simulate the final state of the XA process. The final-state calculation also reproduced accurately the low-energy component of the σ^* peak, called σ_1^* in Ref. 34. The high-energy part of the σ^* peak, σ_2^*, was not reproduced at all. This approach was also less successful in reproducing the relative intensity of the π^* and σ_1^* peaks. It should also be noted that although the peak position and line shape of the π^* and σ_1^* peaks were described in the theory of Ref. 35 quite well, the relative intensity of these peaks was simply fitted to the experimental data.

Also, theoretical work using several levels of approximation has been done for C_{60}.[15,36–38] The XA spectrum of C_{60} has been analyzed in terms of excitations of a $1s$ core electron to a π^* orbital. The π^* orbitals of the carbon atoms hybridize and group into irreducible representations of the icosahedral symmetry group. The first two observed peaks above the threshold are characterized as excitations to orbitals with t_{1u} and t_{1g} symmetry, the third peak corresponds to transitions to the nearly degenerate orbitals with t_{2u} and h_g symmetry.[24] It has been found that in order to reach a good agreement between the XAS data and first-principles computational results it is important to consider the effect of the core hole in the absorption process.[25,27,36] Here we take into account the *dynamical* character of the interaction between the core hole and valence electrons, which in principle should improve the agreement between theory and experiment.

A single-wall carbon nanotube can be considered as a rolled up sheet of graphite. It has been found that the electronic properties of SWCNTs are strongly dependent on the chirality that is specified by the rolling direction and diameter of the tube. The chirality determines whether the tube is a semiconductor or a metal. Also, the fine structure of the density of states is changed with the chirality.[17,18] The manufacturing and purification process of SWCNT materials have been an extremely intense field of research since their discovery.[39] Despite all efforts, large amounts of SWCNTs having exactly the same chirality has been difficult to realize. The XA measurements on SWCNTs have been done on samples with mixed chirality and its spectrum have been found to be very similar to the XA spectrum of graphite.[28] From such measurements it is difficult to obtain any information of the electronic structure for a specific chirality, and no chirality-specific theoretical analysis of the XA spectra of SWCNT systems has been done.

We have therefore carried out a detailed analysis based on the MND theory in combination with an accurate first-principles electronic structure method, both for graphite, C_{60}, a metallic and an insulating SWCNT. As we will demonstrate, our approach describes successfully both the energy positions, spectral shapes, and intensities of the peaks in the XA spectra of these three forms of carbon.

II. COMPUTATIONAL METHOD

The original version of the MND theory is difficult to solve numerically since it requires an integration of the Green function over the whole energy axis. The approach formulated in Ref. 6 involves only the imaginary part of the Green function, which is nonzero only in a restricted energy interval which makes it easier to solve numerically. We have generalized the scheme in Ref. 6 such that it can be applied to a realistic multiband case.

Technically, the computational procedure is as follows. We make use of initial- and final-state retarded Green functions defined as $g^R(\omega)=(\omega-\mu+i\delta-H)^{-1}$, and $G^R(\omega)=(\omega-\mu+i\delta-H-V)^{-1}$, correspondingly. Here μ is the chemical potential, δ is a small complex component to the argument of the Green functions, H is the Hamiltonian,

$$H=\sum_{mn}\sum_{RR'}\tau_{mnRR'}a_{mR}^{\dagger}a_{nR'} \tag{1}$$

and V the core-hole potential

$$V=\sum_{mn}V_{mn}a_{m0}^{\dagger}a_{n0}. \tag{2}$$

In the above equation $a_{nR}^{\dagger}$ and a_{nR} are the creation and annihilation operators for an electron in an orbital at site R with orbital quantum number n, the core hole is created on the site with $R=0$ and $\tau_{mnRR'}$ is the hopping integral. The operators in Eqs. (1) and (2) are a generalization of the operators in Eq. (6) of Ref. 6. In Ref. 6, Eq. (6) is the interaction between a valence hole and the core electrons included and the total Hamiltonian is expressed using the creation and annihilation operators of a core hole $b^{\dagger}$ and b,

$$H_{\mathrm{tot}}=\sum_{mn}\sum_{RR'}\tau_{mnRR'}a_{mR}^{\dagger}a_{nR'}+\epsilon_c b^{\dagger}b+\sum_{mn}V_{mn}a_{m0}^{\dagger}a_{n0}bb^{\dagger}. \tag{3}$$

We assume that the core electron excited in the XA process undergoes a transition to some orbital at the same absorbing atom. The electronic structure of the latter is described by the projections of the Green functions on to local orbitals m,n, as $\mathbf{g}_{mn}^R=\langle m|g^R|n\rangle$ and $\mathbf{G}_{mn}^R=\langle m|G^R|n\rangle$.

The initial- and final-state Green functions are connected by the Slater-Koster equation

$$G^R(\omega)=g^R(\omega)+g^R(\omega)VG^R(\omega). \tag{4}$$

The corresponding equation for the locally projected quantities reads

$$\begin{aligned}\langle m|G^R(\omega)|n\rangle &= \langle m|g^R(\omega)|n\rangle+\langle m|g^R(\omega)VG^R(\omega)|n\rangle\\ &= \mathbf{g}_{mn}^R(\omega)+\langle m|g^R(\omega)\Big(\sum_{i,j}|i\rangle\langle i|V|j\rangle\langle j|\\ &\quad -\sum_{i,j}|i\rangle\langle i|V|j\rangle\langle j|+V\Big)G^R(\omega)|n\rangle\\ &= \mathbf{g}_{mn}^R(\omega)+[\mathbf{g}^R(\omega)\mathbf{V}\mathbf{G}^R(\omega)]_{mn}\end{aligned}$$

$$+\langle m|g^R(\omega)\left(V-\sum_{i,j}|i\rangle\langle i|V|j\rangle\langle j|\right)G^R(\omega)|n\rangle. \tag{5}$$

Equation (4) can also be written as

$$G^R(\omega)=g^R(\omega)[1-Vg^R(\omega)]^{-1}, \tag{6}$$

and the corresponding equation for locally projected quantities takes the form

$$\mathbf{G}^R(\omega)=\mathbf{g}^R(\omega)\{1-[\mathbf{V}+\tilde{\mathbf{V}}(\omega)]\mathbf{g}^R(\omega)\}^{-1},$$

$$\tilde{\mathbf{V}}(\omega)=[\mathbf{g}^R(\omega)]^{-1}\tilde{\mathbf{W}}(\omega)[\mathbf{G}^R(\omega)]^{-1},$$

$$\tilde{\mathbf{W}}_{mn}(\omega)=\langle m|g^R(\omega)\left(V-\sum_{ij}|i\rangle\mathbf{V}_{ij}\langle j|\right)G^R(\omega)|n\rangle. \tag{7}$$

For a *complete* set of local orbitals $\tilde{\mathbf{V}}=\mathbf{0}$, so that the effective potential is not energy dependent. For a nonenergy dependent effective potential the scheme in Ref. 6 can easily be generalized to the multiband case.

The XAS intensity function $I(\omega)$ is now given by the expression[6]

$$I(\omega)\sim \mathrm{Re}\int_0^\infty dt\int_\mu^\infty \frac{d\epsilon}{\pi}e^{it(\omega-\epsilon+\epsilon_c)+\Delta(-t)} \times\sum_{ij}t_i[\mathrm{Im}\,\mathbf{g}^R(\epsilon)\tilde{\boldsymbol{\varphi}}(\epsilon,t)]_{ij}t_j^*, \tag{8}$$

where $t_n=\mathbf{E}\cdot\langle 1s|\mathbf{p}|n\rangle$, $\mathbf{E}$ is the x-ray electric field, $\mathbf{p}$ is the dipole moment operator (to be specific, we consider the K spectrum where the core state is a $1s$ orbital of the C atom) and ϵ_c is the energy of the core state. The function $\Delta(-t)$ contains in general[6] the core-state energy shift, and the core-hole finite lifetime is determined by the expression

$$\Delta(t)=i\,\mathrm{Tr}\,\mathbf{V}\int_0^{-t}dt_1\int_{-\infty}^{\mu}\frac{d\epsilon}{\pi}\,\mathrm{Im}\,\mathbf{g}^R(\epsilon)\tilde{\boldsymbol{\varphi}}(\epsilon,t_1), \tag{9}$$

where $\tilde{\boldsymbol{\varphi}}(\epsilon,t)$ can be found from the matrix integral equation

$$\tilde{\boldsymbol{\varphi}}(\epsilon,t)=\mathbf{1}+\mathbf{V}\int_\mu^\infty\frac{d\epsilon_1}{\pi}\,\mathrm{Im}\,\mathbf{g}^R(\epsilon_1)\mathbf{L}^+(\epsilon,\epsilon_1,t)\tilde{\boldsymbol{\varphi}}(\epsilon_1,t),$$

$$\mathbf{L}^+(\epsilon,\epsilon_1,t)=\frac{\mathbf{I}^*(\epsilon_1,t)-e^{i(\epsilon-\epsilon_1)t}\mathbf{I}^*(\epsilon,t)}{\epsilon_1-\epsilon},$$

$$\mathbf{I}(\epsilon,t)=\mathbf{1}+\mathbf{V}\int_{-\infty}^{\infty}\frac{d\epsilon_1}{\pi}\frac{e^{i(\epsilon-\epsilon_1)t}-1}{\epsilon-\epsilon_1}\,\mathrm{Im}\,\mathbf{G}^R(\epsilon_1). \tag{10}$$

($*$ means the complex conjugation of all matrix elements).

III. NUMERICAL IMPLEMENTATION

The input for the MND calculation $\mathbf{G}^R$, $\mathbf{g}^R$, and $\mathbf{V}$ can be obtained from first-principles band theory as follows. We calculate the projections of the Bloch wave functions with the wave-vector $\mathbf{k}$ and the band index l onto the spherical harmonics with angular momentum numbers m centered on site a, that is, $\langle\mathbf{k},l|a,m\rangle$ using first-principles band theory. The projections must be normalized

$$\sum_{\mathbf{k},l}|\langle\mathbf{k},l|a,m\rangle|^2=1 \tag{11}$$

in order to calculate the Green function

$$\mathbf{G}^R_{mn}(\epsilon)=\sum_{\mathbf{k},l}\frac{\langle a,m|\mathbf{k},l\rangle\langle\mathbf{k},l|a,n\rangle}{\epsilon-\epsilon_{\mathbf{k},l}-\mu+i\delta}. \tag{12}$$

In this expression $\epsilon_{\mathbf{k},l}$ are the energies of the Bloch state with the quantum numbers $\mathbf{k}$ and l. The final-state Green function is calculated using a supercell with a core hole at site a. The Green function is considered to be a function of a discrete energy variable $\epsilon\in\{\epsilon_{\min}-\alpha\Delta\epsilon|\,\alpha=0,1,\ldots,N\}$. Such a Green function can be represented by a block vector where each element $\mathbf{G}^R_\alpha=\mathbf{G}^R(\epsilon_{\min}-\alpha\Delta\epsilon)$ is a matrix with the orbital index m,n. The mesh of the energy points $\{\epsilon_{\min}-\alpha\Delta\epsilon|\,\alpha=0,1,\ldots,N\}$ must cover the valence band and the broadening of the energy levels, δ, should be larger than the distance between points in the energy mesh, $\Delta\epsilon$.

The core-hole potential can be obtained using the expression

$$\begin{aligned}V&=[g^R(\omega)]^{-1}-[G^R(\omega)]^{-1}\\&=\sum_{\mathbf{k},l'}|\mathbf{k},l'\rangle\langle\mathbf{k},l'|(\omega-\epsilon_{\mathbf{k},l'}-\mu+i\delta)\\&\quad-\sum_{\mathbf{k},l}|\mathbf{k},l\rangle\langle\mathbf{k},l|(\omega-\epsilon_{\mathbf{k},l}-\mu+i\delta)\\&=\sum_{\mathbf{k},l}|\mathbf{k},l\rangle\langle\mathbf{k},l|\epsilon_{\mathbf{k},l}-\sum_{\mathbf{k},l'}|\mathbf{k},l'\rangle\langle\mathbf{k},l'|\epsilon_{\mathbf{k},l'},\end{aligned} \tag{13}$$

where $|\mathbf{k},l'\rangle,\epsilon_{\mathbf{k},l'}$ and $|\mathbf{k},l\rangle,\epsilon_{\mathbf{k},l}$ are eigenstates and eigenenergies of the initial-state Hamiltonian, H, and the final-state Hamiltonian, $H+V$, respectively. The eigenstates and eigenenergies can be found by supercell calculations, with and without the core hole. The expression for the core-hole potential, V, projected on local orbital reads

$$\begin{aligned}\mathbf{V}_{m,n}&=\sum_{\mathbf{k},l}\langle a,m|\mathbf{k},l\rangle\langle\mathbf{k},l|a,n\rangle\epsilon_{\mathbf{k},l}\\&\quad-\sum_{\mathbf{k},l'}\langle a,m|\mathbf{k},l'\rangle\langle\mathbf{k},l'|a,n\rangle\epsilon_{\mathbf{k},l'},\end{aligned} \tag{14}$$

where a is the site with the core hole. In practice only one calculation is needed, and $\mathbf{V}$ can be obtained from the expression

$$\mathbf{V}_{m,n}=\sum_{\mathbf{k},l}(\langle a_1,m|\mathbf{k},l\rangle\langle\mathbf{k},l|a_1,n\rangle-\langle a_2,m|\mathbf{k},l\rangle\langle\mathbf{k},l|a_2,n\rangle)\epsilon_{\mathbf{k},l}, \tag{15}$$

where a_1 is an atomic site with the core hole and a_2 is an equivalent site situated sufficiently far away from the core hole. The initial-state Green function can be obtained from the expression $\mathbf{g}^R_\alpha=\mathbf{G}^R_\alpha(1+\mathbf{V}\mathbf{G}^R_\alpha)^{-1}$, which is the inverse of Eq. (7) assuming that $\tilde{\mathbf{V}}=0$.

The function $\mathbf{I}(\epsilon,t)$ in Eq. (10) is also represented as a block vector where each element $\mathbf{I}_\alpha(t)$ is a matrix and

$$\mathbf{I}_\alpha(t) = \mathbf{1} + \mathbf{V}\sum_\beta \frac{\Delta\epsilon}{\pi}\frac{e^{i[(\alpha-\beta)\Delta\epsilon]t}-1}{(\alpha-\beta)\Delta\epsilon}\,\mathrm{Im}\,\mathbf{G}^R_\beta. \tag{16}$$

The sampling theorem states that in order to sample a function the sampling frequency must be twice the maximal frequency of the function which is a restriction on the maximum value of t that can be represented using a discrete energy mesh, that is, $t_{\max}=\pi/\Delta\epsilon$.

If we represent $\tilde{\boldsymbol{\varphi}}(\epsilon,t)$ by a block vector $\bar{\boldsymbol{\varphi}}_\alpha(t)=\tilde{\boldsymbol{\varphi}}(\epsilon_{\min}-\alpha\Delta\epsilon,t)$ then Eq. (10) takes the form

$$\bar{\boldsymbol{\varphi}}(t) = \bar{\mathbf{A}} + \bar{\bar{\mathbf{B}}}(t)\bar{\boldsymbol{\varphi}}(t). \tag{17}$$

In the above equation $\bar{\bar{\mathbf{B}}}$ is a supermatrix where the elements $\bar{\bar{\mathbf{B}}}_{\alpha\beta}$ are matrices given by the expression

$$\bar{\bar{\mathbf{B}}}_{\alpha\beta}(t) = \mathbf{V}\frac{\Delta\epsilon}{\pi}\,\mathrm{Im}(\mathbf{g}^R_\beta)\frac{\mathbf{I}^*_\beta(t)-e^{i(\alpha-\beta)\Delta\epsilon}\mathbf{I}^*_\alpha(t)}{(\beta-\alpha)\Delta\epsilon}\theta(\epsilon_{\min}+\beta\Delta\epsilon-\mu)$$

$$\theta(x) = \begin{cases} 0, & x<0, \\ 1, & x\geqslant 0. \end{cases} \tag{18}$$

The elements of the block vector $\bar{\mathbf{A}}$ in Eq. (17) are unit matrices. We can now solve Eq. (17) for $\bar{\boldsymbol{\varphi}}(t)$,

$$\bar{\boldsymbol{\varphi}}(t) = [\bar{\bar{\mathbf{1}}} - \bar{\bar{\mathbf{B}}}(\omega)]^{-1}\bar{\mathbf{A}}. \tag{19}$$

In order to calculate numerically the integrals in Eqs. (8) and (9) the argument of $\bar{\boldsymbol{\varphi}}_\alpha(t)$, i.e., t, should also be discretized. The time mesh $t\in\{\gamma\Delta t\,|\,\gamma=0,1,\ldots,M\}$ is chosen by the following considerations. If we represent the integral $\int(d\epsilon/\pi)e^{-it\epsilon}$ in Eq. (8) as a discrete Fourier transform over the energy interval $\epsilon_{\min}-(\epsilon_{\min}+N\Delta\epsilon)$, it is natural to represent the integral $\int dt e^{it\omega}$ as an inverse discrete Fourier transform. This implies that the distance between points in the time mesh is related to the distance between points in the energy mesh by the expression $\Delta t=2\pi/[(N+1)\Delta\epsilon]$.

We can now calculate numerically the XAS intensity function using a discrete version of Eq. (8),

$$I(\omega) \sim \mathrm{Re}\sum_{\gamma,0\leqslant\gamma\leqslant t_{\max}/\Delta t}\Delta t\sum_\alpha \theta(\epsilon_{\min}+\alpha\Delta\epsilon-\mu) \times\frac{\Delta\epsilon}{\pi}e^{it(\omega-\alpha\Delta\epsilon+\epsilon_c)+\Delta(-\gamma\Delta t)}\sum_{ij} t_i[\mathrm{Im}\,\mathbf{g}^R_\alpha\bar{\boldsymbol{\varphi}}_\alpha(\gamma\Delta t)]_{ij}t^*_j. \tag{20}$$

The first sum in the above expression is a sum over the time mesh, this sum is truncated at $t_{\max}$ since higher values of t cannot be represented within the resolution of the energy mesh. The function $\Delta(-\gamma\Delta t)$ in Eq. (20) is calculated numerically using the expression

$$\Delta(-\gamma\Delta t) = i\,\mathrm{Tr}\,\mathbf{V}\sum_{\eta,0\leqslant\eta\leqslant\gamma}\Delta t\sum_\alpha\theta(\mu-\epsilon_{\min}-\alpha\Delta\epsilon) \times\frac{\Delta\epsilon}{\pi}\,\mathrm{Im}(\mathbf{g}^R_\alpha)\bar{\boldsymbol{\varphi}}_\alpha(\eta\Delta t), \tag{21}$$

and ϵ_c is used as a fitting parameter since the core electrons are considered using a pseudopotential.

IV. FIRST-PRINCIPLES CALCULATIONS

In order to evaluate the material-specific quantities of graphite, C_{60}, and the carbon nanotubes, according to Eqs. (8)–(10), we have performed first-principles calculations based on the plane-wave VASP code[40] within the projector augmented wave (PAW)[41] method. The exchange-correlation energy was described by the Ceperley and Alder functional[42] parametrized by Perdew and Zunger.[43] We note that the particular form of the functional used does not influence the electronic structure of the materials studied here, or materials in general. As an example we note that we obtain a very similar ground state electronic structure here as the one presented in Ref. 11, where the Hedin-Lundqvist functional was used. The Monkhorst-Pack scheme[44] was applied to generate special k-points. For the case of graphite we used a supercell with 144 carbon atoms arranged in two graphite layers and a $5\times5\times1$ k-point mesh. For the case of C_{60} a simple cubic supercell with 60 carbon atoms arranged in the fullerene structure and a $2\times2\times2$ k-point mesh were used. Calculations were made for two types of SWCNTs with a diameter of $\sim$12 Å, one predicted to be metallic and one predicted to be a narrow band semiconductor.[28] Using the notation of Ref. 18 the chirality for the tubes were (9,9) and (15,0), respectively. For the metallic nanotube a tetragonal supercell of 72 atoms and a $1\times1\times2$ k-point mesh was used. For the semiconducting nanotube a 60 atom tetragonal supercell and a $1\times1\times2$ k-point mesh was used. Since graphite, C_{60}, and SWCNTs are open structures, special care was taken to converge the calculation with respect to plane-wave energy cutoff. In all calculations a 400 eV kinetic energy cutoff was used for the plane waves in the basis set. Since the radius of the $1s$ state is much smaller than that of $2p$, effectively the action of the core hole on the valence band is equivalent to the change of the nuclei charge Z by $Z+1$ for one atom in our supercells.[45] After the replacement of a carbon atom by nitrogen we let the electrons (including the extra valence electron of the N atom) self-consistently relax to the new "ground state." The plane-wave components of the eigenstates were projected onto spherical harmonics inside the PAW spheres in order to obtain the projections $\langle\mathbf{k},l\,|\,a,m\rangle$ that were used in Eq. (12) to calculate the Green functions. The radius of the spheres is 0.8 Å. The locally projected quantities $\mathbf{g}^R,\mathbf{G}^R,\mathbf{V}$ are 4×4, matrices since the projections are made on s,p_1,p_0,p_{-1} orbitals $[p_1=1/\sqrt{2}(-p_x-ip_y)$, $p_0=p_z$, $p_{-1}=1/\sqrt{2}(p_x-ip_y)]$.

From the first-principles scheme described above both the initial- and final-state spectra were calculated. The initial-state spectra were given by the estimate $I^i(\omega)\sim\Sigma_{ij}t_i\,\mathrm{Im}\,\mathbf{g}^R_{ij}t^*_j$. The final-state spectra $I^f(\omega)$ were obtained in the same way

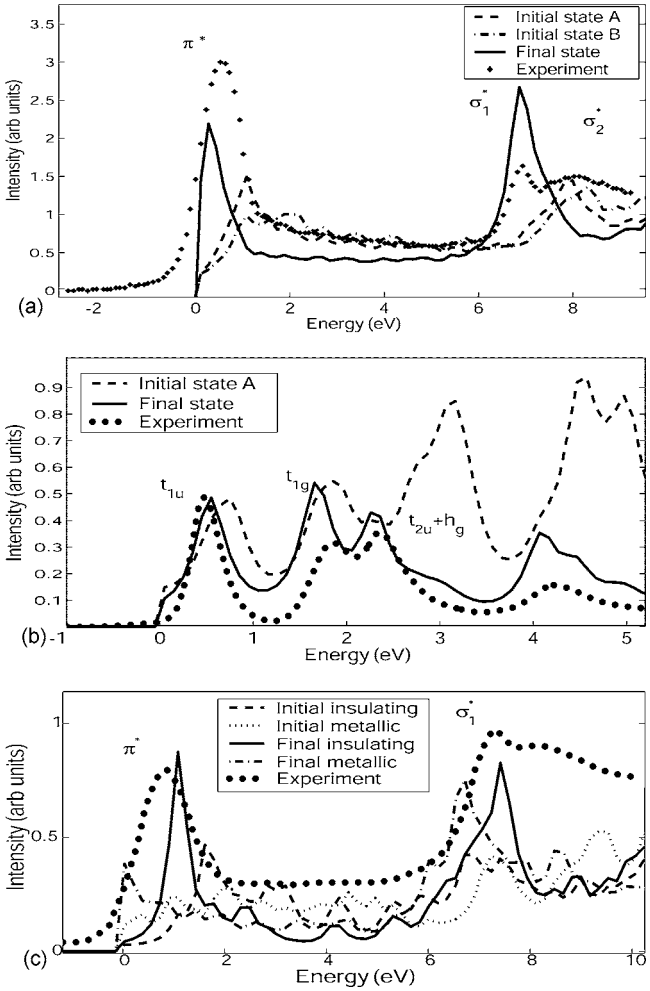

FIG. 1. Theoretical and experimental XA spectra of graphite are displayed in (a). The experimental data (Ref. 34) are shown by diamonds. The solid line is the final-state spectrum. The dashed-dotted line is the spectrum obtained from projections made on a site without a core hole (named initial state B). The dashed line is the spectrum obtained using the inverse of Eq. (7) with $\tilde{\mathbf{V}}=\mathbf{0}$ (named initial state A). The theoretical and experimental XA spectra of C_{60} are shown in (b). The circles are the experimental spectrum (Ref. 24). The full line is the spectrum obtained from projections made on a site with a core hole. The dashed line is the spectrum obtained using the inverse of Eq. (7) with $\tilde{\mathbf{V}}=\mathbf{0}$. The theoretical and experimental XA spectra of the SWCNTs are shown in (c). The circles are the experimental spectrum (Ref. 28). The full and dashed-dotted lines are the spectra obtained from projections made on a site with a core hole for the semiconducting and metallic tubes, respectively. The dashed and the dotted lines are the spectra obtained using the inverse of Eq. (7) with $\tilde{\mathbf{V}}=\mathbf{0}$ for the semiconducting and metallic tubes, respectively. For further details see the text.

using $\mathbf{G}^R$ instead of $\mathbf{g}^R$. Figures 1(a)–1(c) show the computed results of $I^i(\omega)$ and $I^f(\omega)$ for graphite, C_{60} and SWCNTs respectively, together with the experimental spectra taken from Refs. 24, 34, and 28. In the SWCNT experiment the nanotubes in the sample had mixed chirality but a diameter of approximately 12 Å.

In the case of graphite the experimental spectrum was measured for x rays polarized in such a way that the electric field $\mathbf{E}$ is parallel to the plane of incidence and the x rays are incident at the angle of 45° to the graphite planes.[34] This configuration corresponds to $t_n \sim 0,1,\sqrt{2},1$ for $n=s,p_1,p_0,p_{-1}$. Due to the high symmetry of the C_{60} molecule all parameters t_n can be set equal (except for $t_s=0$, since dipole selection prohibits this transition). The experimental spectrum of the SWCNTs were taken using a sample with randomly aligned nanotubes[28] and thus at t_n were again set to be equal (except for $t_s=0$) in the theoretical calculations of the spectrum.

In comparison with the experimental spectrum the computational initial- and final-state results, $I^i(\omega)$ and $I^f(\omega)$, respectively, do not reproduce the shape and the intensity of the experimental spectrum, although we note that the curve $I^f(\omega)$ describes roughly the correct peak positions. This observation holds both for graphite, C_{60}, and the SWCNTs.

Also, one should note that there are two ways to calculate the locally projected initial-state Green function which would be identical only for the complete orbital basis set. The first one is to use Eq. (12) with the projections made on a site without the core hole, and the second one is to use the inverse of Eq. (7) with $\tilde{\mathbf{V}}=0$. As it is shown in Fig. 1(a) and Fig. 2 the difference between these two results for $I^i(\omega)$ is small, which justifies our assumption that the basis set is sufficiently large to neglect $\tilde{\mathbf{V}}$. This conclusion holds for the calculations of graphite, C_{60}, and the SWCNTs.

V. RESULTS FOR GRAPHITE

Figure 3 displays the XA spectrum for graphite calculated using Eq. (20). It is clearly seen that the positions of the π^* and σ_1^* peaks are reproduced very well by the theory. Of practical importance is the fact that the relative intensities of the π^* and σ_1^* peaks are drastically improved compared to the final-state spectrum [see Fig. 1(a)]. In Fig. 3 the theoretical curves have been broadened with a Gaussian of width 0.5 eV, to make the comparison with the experimental data more appropriate.

From Fig. 3 it may be seen that the spectral features labeled π^* and σ_1^* are reproduced well by our theory. However, the σ_2^* peak is not reproduced by the spectrum calculated using Eq. (20). We have taken into account the effects of dynamical screening of the core hole, using the MND theory, and in addition evaluated the final-state spectrum in the most accurate way, i.e., by a self-consistent, material specific method, with the inclusion of a core hole. We thus must conclude that the mechanism responsible for the σ_2^* peak is beyond the MND theory. In the concluding section of this paper this problem is analyzed in more detail. However, we do note that the present calculation is an improvement in comparison with completely static initial- or final-state calculations, which is a quite essential result.

VI. RESULTS FOR C_{60}

Figure 4 displays the spectrum for C_{60} calculated using Eq. (20), and it is clearly seen that the positions of the t_{1u}, t_{1g}, and $t_{2h}+h_g$ peaks are reproduced very well by the theory. A comparison between the MND theory and the final-state

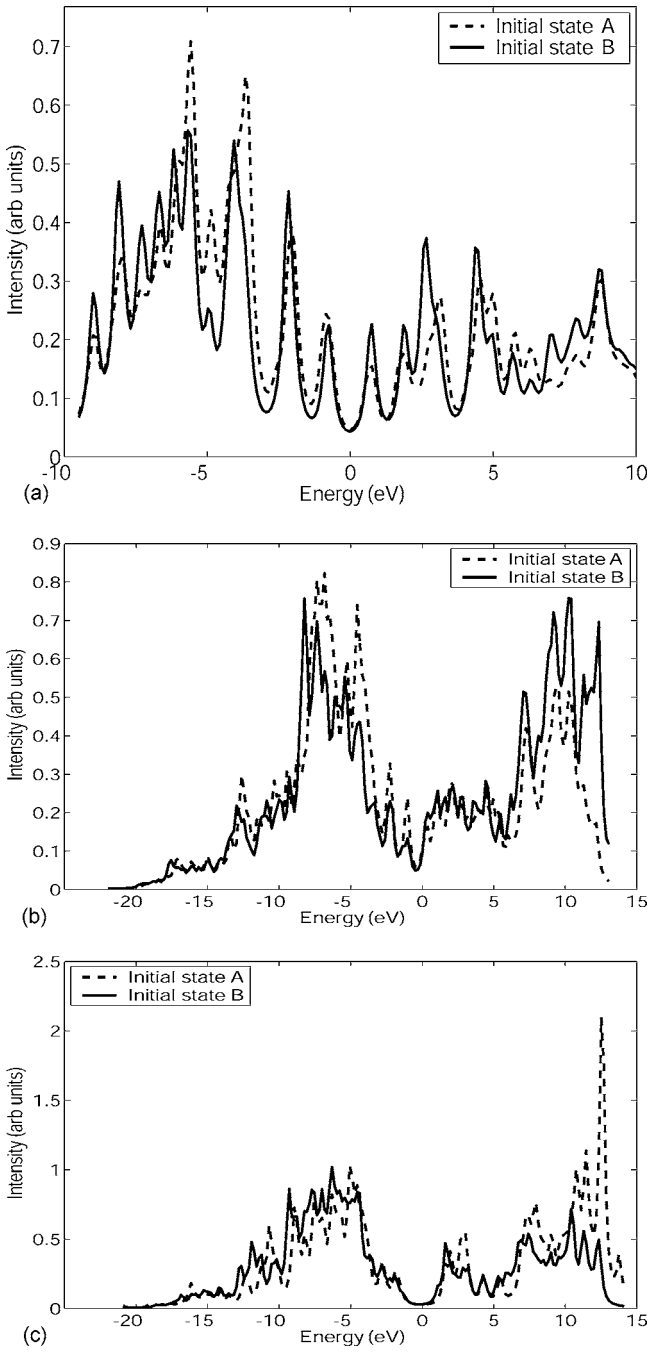

FIG. 2. Initial state spectra of C_{60}, metallic SWCNT and semiconducting SWCNT are shown in (a), (b), and (c), respectively. Both occupied and unoccupied states are shown and the Fermi level is at zero energy. The full lines are spectra obtained from projections made on a site without a core hole. The dashed lines are spectra obtained using the inverse of Eq. (7) with $\tilde{\mathbf{V}}=\mathbf{0}$. For further details see the text.

approximation [Fig. 1(b)] gives as the main difference that the relative intensities are better described with the MND theory. It is in particular the relative intensity between the t_{1u} and t_{1g} peaks that in the MND theory is drastically improved compared to the final-state calculations. The only inaccuracy one may observe from this theory is that the t_{1g} peak does not have quite correct intensity relative to the $t_{2h}+h_g$ peak.

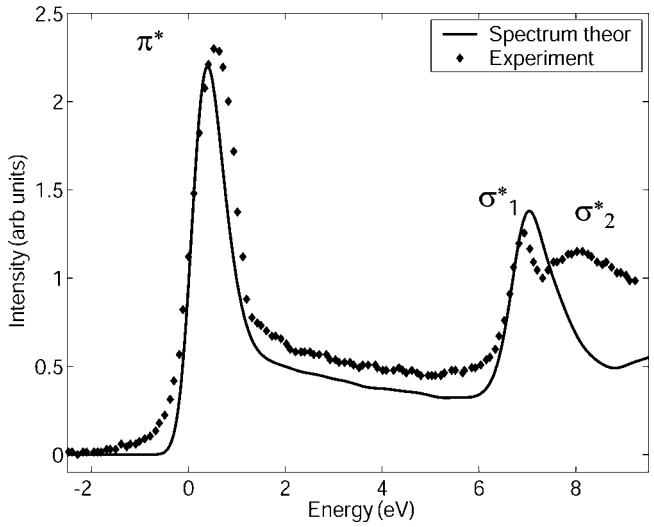

FIG. 3. Theoretical and experimental XA spectra of graphite. The theoretical results were calculated by Eq. (20).

This effect can possibly be related to the fact that the $Z+1$ approximation does not correctly describe the shape of the core hole as shown in Ref. 36, Fig. 2. However, the feature at 4 eV above threshold is reproduced almost perfectly from the MND theory, whereas the final-state approximation produces a much too large intensity.

We also note here that even though we carefully converged our calculation with respect to the size of our basis set, the present calculation gives a final-state spectrum that is somewhat different than that presented in Ref. 36. We speculate that a plausible reason is that the calculation in Ref. 36 uses different values of the dipole transition matrix elements t_n.

VII. RESULTS FOR THE SWCNTS

Figure 5 displays the XA spectra for a metallic (9,9) and a semiconducting (15,0) SWCNT calculated using Eq. (20).

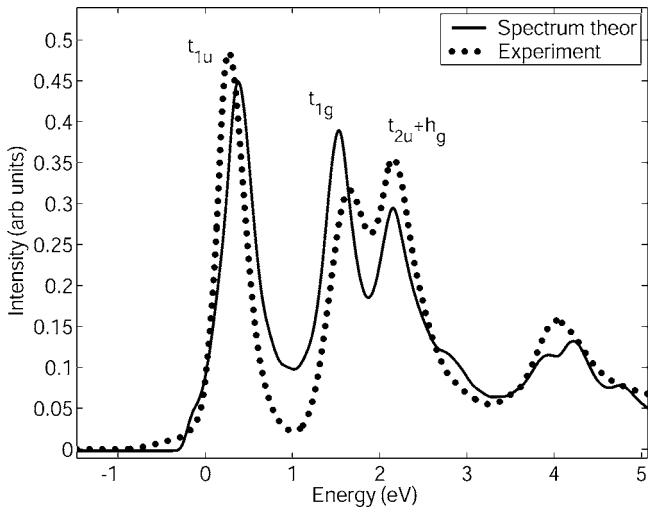

FIG. 4. Theoretical and experimental XA spectra of C_{60}. The theoretical results were calculated by Eq. (20).

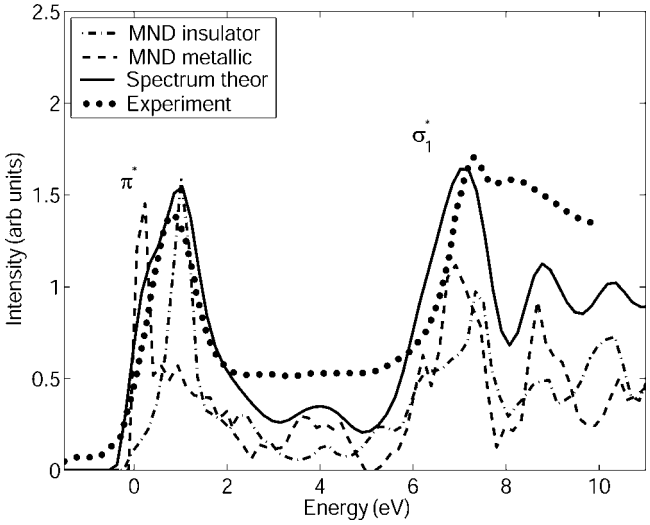

FIG. 5. Theoretical and experimental XA spectra of SWCNTs. The circles are the experimental spectrum (Ref. 28). The dashed and the dashed-dotted lines are the spectra calculated using Eq. (20) for the metallic and the semiconducting nanotubes, respectively. The solid line is the mean of the dashed and the dashed-dotted lines broadened with a Gaussian of 0.5 eV.

From Fig. 5 it is clear that the position of the π^* peak in the XA spectrum of a single SWCNT is strongly dependent on the chirality. The MND spectrum of the metallic nanotube has a peak at the threshold whereas the semiconducting nanotube has a peak 1 eV above the threshold. The experimental spectra in Fig. 5 are obtained using a sample where the chirality is not well defined but the distribution of diameters of the nanotubes in the sample is strongly peaked at 12 Å (Refs. 28 and 29), and that is, as mentioned, the diameter used in our calculations. Neither the theoretical spectra of the semiconducting or metallic nanotubes would alone be able to reproduce both the shape and the position of π^* and σ^* peaks of the experimental spectrum. However, a superposition of the two theoretical spectra, which is also shown in Fig. 5, agrees rather well with the experiment. We speculate that the peaks at 4, 9, and 10 eV that are only present in the theoretical spectrum would disappear if more SWCNTs with different chirality and a distribution of diameters close to 12 Å (the experimental situation) were included in the theoretical calculation of the spectrum.

VIII. CONCLUSIONS

We have shown that first-principles electronic structure calculations can be combined with multiband MND theory to a computational scheme that includes the dynamical response of the valence electrons to the creation of a core hole in the XA process. Our method has been compared with the commonly used final-state approximation and, in agreement with the final-state rule,[1] it was found that the peak positions of the spectra but not the spectral weights are given by the final-state density of states. However, we note that it is indeed the relative intensities between features with different symmetry (e.g., the π^* and σ^* states of graphite and t_{1u} and t_{1g} states of C_{60}) that become drastically improved with the present method. We expect that it is for systems that in this sense are similar to graphite and C_{60}, with several spectroscopic features with different symmetry, where the present approach will be especially useful.

The final-state approach considers the appearance of the core potential as an *adiabatically slow* process which can be justified only in the ladder approximation,[4] that is, only for insulators or semiconductors and only with an assumption that one can neglect the effect of the core hole on the occupied valence band. One can see from our results that the latter does not hold for carbon systems. The only assumption that is made when applying the MND theory together with first-principle calculations is that the formation of the core-hole potential V is supposed to be an instant process. This means that we consider the effect of an instant shake-up process, that is, a creation of the hole, in a proper dynamic way. Formally speaking, the only not completely controllable assumption that is made is the adiabatic approximation for the exchange-correlation potential; that is, we do not use the rigorous *time-dependent* density functional method. Probably the theory should be further developed in this direction to overcome the small error that in the present approach exists compared to experiment.

We have also found that the XA spectrum of a SWCNT is sensible to the chirality of the tube and this suggests that XAS could be used as a chirality probe. Finally, our results show that for most of the components of the XA spectrum in graphite the MND theory works very successfully, and that only the σ_2^* peak appears to be *completely screened* very quickly so that it is described by the initial-state density of states, as was discussed in Ref. 19. It should be noted that this peak has also been interpreted in experimental works to be the result of a delocalized excitation.[34]

ACKNOWLEDGMENTS

Support from the Swedish Natural Research Council (VR) and the foundation for strategic research (SSF) is acknowledged. We also acknowledge support from the Swedish National Super Computer Facility (NSC) and the Center for Dynamical Processes, Uppsala University. One of the authors (O. E.) is grateful to the Göran Gustafsson foundation.

[1] U. von Barth and G. Grossmann, Phys. Scr. **21**, 580 (1980).
[2] A. L. Ankudinov, A. I. Nesvizhskii, and J. J. Rehr, Phys. Rev. B **67**, 115120 (2003); H. Modrow, S. Bucher, J. J. Rehr, and A. L. Ankudinov, *ibid.* **67**, 035123 (2003).
[3] E. L. Shirley, Phys. Rev. Lett. **80**, 794 (1998).
[4] G. D. Mahan, *Many-Particle Physics* (Plenum, New York, 1990), Chap. 8.
[5] P. Nozières and C. T. De Dominicis, Phys. Rev. **178**, 1097 (1969).
[6] V. I. Grebennikov, Yu. A. Babanov, and O. B. Sokolov, Phys. Status Solidi B **79**, 423 (1977).
[7] T. Privalov, F. Gel'mukhanov, and H. Ågren, Phys. Rev. B **64**, 165115 (2001).
[8] H. Ebert, J. Stöhr, S. S. P. Parkin, M. Samant, and A. Nilsson, Phys. Rev. B **53**, 16067 (1996); I. Galanakis, S. Ostanin, M. Alouani, H. Dreyssé, and J. M. Wills, *ibid.* **61**, 4093 (2000).
[9] F. M. F. de Groot, J. C. Fuggle, B. T. Thole, and G. A. Sawatzky, Phys. Rev. B **42**, 5459 (1990); J. Zaanen, G. A. Sawatzky, J. Fink, W. Speier, and J. C. Fuggle, *ibid.* **32**, 4905 (1985).
[10] O. Karis, M. Magnuson, T. Wiell, M. Weinelt, N. Wassdahl, A. Nilsson, N. Mårtensson, E. Holmström, A. M. N. Niklasson, O. Eriksson, and B. Johansson, Phys. Rev. B **63**, 113401 (2001).
[11] R. Ahuja, S. Auluck, J. M. Wills, M. Alouani, B. Johansson, and O. Eriksson, Phys. Rev. B **55**, 4999 (1997).
[12] H. J. F. Jansen and A. J. Freeman, Phys. Rev. B **35**, 8207 (1987).
[13] N. A. W. Holzwarth, S. G. Louie, and S. Rabii, Phys. Rev. B **26**, 5382 (1982).
[14] J.-C. Charlier, X. Gonze, and J.-P. Michenaud, Phys. Rev. B **43**, 4579 (1991).
[15] N. Troullier and J. L. Martins, Phys. Rev. B **46**, 1754 (1992).
[16] S. Reich, C. Thomsen, and P. Ordejón, Phys. Rev. B **65**, 155411 (2002).
[17] J. T. Titantah, K. Jorissen, and D. Lamoen, Phys. Rev. B **69**, 125406 (2004).
[18] M. S. Dresselhaus, G. Dresselhaus, and P. C. Eklund, *Science of Fullerenes and Carbon Nanotubes* (Academic, San Diego, 1996).
[19] O. Wessely, M. I. Katsnelson, and O. Eriksson, Phys. Rev. Lett. **94**, 167401 (2005).
[20] H. W. Kroto, J. R. Heath, S. C. O'Brien, R. F. Curl, and R. E. Smalley, Nature (London) **318**, 162 (1985).
[21] S. Iijima, Nature (London) **354**, 56 (1991).
[22] P. Skytt, P. Glans, D. C. Mancini, J.-H. Guo, N. Wassdahl, J. Nordgren, and Y. Ma, Phys. Rev. B **50**, 10457 (1994).
[23] R. A. Rosenberg, P. J. Love, and V. Rehn, Phys. Rev. B **33**, 4034 (1986).
[24] A. Goldoni, L. Sangaletti, F. Parmigiani, S. L. Friedmann, Z.-X. Shen, M. Peloi, G. Comelli, and G. Paolucci, Phys. Rev. B **59**, 16071 (1999).
[25] B. Wästberg, S. Lunell, C. Enkvist, P. A. Brühwiler, A. J. Maxwell, and N. Mårtensson, Phys. Rev. B **50**, 13031 (1994).
[26] P. A. Brühwiler, A. J. Maxwell, P. Rudolf, C. D. Gutleben, B. Wästberg, and N. Mårtensson, Phys. Rev. Lett. **71**, 3721 (1993).
[27] A. J. Maxwell, P. A. Brühwiler, D. Arvanitis, J. Hasselström, and N. Mårtensson, Phys. Rev. Lett. **79**, 1567 (1997).
[28] S. Eisebitt, A. Karl, W. Eberhardt, J. E. Fischer, C. Sathe, A. Agui, and J. Nordgren, Appl. Phys. A: Mater. Sci. Process. **67**, 89 (1998).
[29] J. Schiessling, L. Kjelgaard, F. Rohmund, L. K. L. Falk, E. E. B. Campbell, J. Nordgren, and P. A. Brühwiler, J. Phys.: Condens. Matter **15**, 6563 (2003).
[30] J. W. McClure, Phys. Rev. **108**, 612 (1957).
[31] J. C. Slonczewski and P. R. Weiss, Phys. Rev. **109**, 272 (1958).
[32] G. S. Painter and D. E. Ellis, Phys. Rev. B **1**, 4747 (1970).
[33] W. A. Harrison, *Electronic Structure, and Properties of Solids* (Dover, New York, 1989).
[34] P. A. Brühwiler, A. J. Maxwell, C. Puglia, A. Nilsson, S. Andersson, and N. Mårtensson, Phys. Rev. Lett. **74**, 614 (1995).
[35] R. Ahuja, P. A. Brühwiler, J. M. Wills, B. Johansson, N. Mårtensson, and O. Eriksson, Phys. Rev. B **54**, 14396 (1996).
[36] M. Nyberg, Y. Luo, L. Triguero, L. G. M. Pettersson, and H. Ågren, Phys. Rev. B **60**, 7956 (1999).
[37] G. Dresselhaus, M. S. Dresselhaus, and P. C. Eklund, Phys. Rev. B **45**, 6923 (1992).
[38] P. Joyes and R. J. Tarento, Phys. Rev. B **49**, 5003 (1994).
[39] A. G. Rinzler, J. Liu, H. Dai, P. Nikolaev, C. B. Huffman, F. J. Rodríguez-Macías, P. J. Boul, A. H. Lu, D. Heymann, D. T. Colbert, R. S. Lee, J. E. Fischer, A. M. Rao, P. C. Eklund, and R. E. Smalley, Appl. Phys. A: Mater. Sci. Process. **67**, 29 (1998).
[40] G. Kresse and J. Hafner, Phys. Rev. B **47**, R558 (1993); G. Kresse and J. Furthmüller, *ibid.* **54**, 11169 (1996).
[41] P. E. Blöchl, Phys. Rev. B **50**, 17953 (1994).
[42] D. M. Ceperley and B. J. Alder, Phys. Rev. Lett. **45**, 566 (1980).
[43] J. P. Perdew and A. Zunger, Phys. Rev. B **23**, 5048 (1981).
[44] H. J. Monkhorst and J. D. Pack, Phys. Rev. B **13**, 5188 (1976).
[45] B. Johansson and N. Mårtensson, Phys. Rev. B **21**, 4427 (1980).